

Self-powered broadband photodetector based on pyramid-structured Si/TiO_2 heterojunction

Leyao Wu(吴乐瑶), Xinnan Shi(师馨楠), Haibo Fan(范海波), Qiujie Li(李秋洁), Peng Hu(胡鹏), and Feng Teng(滕凤)

Citation: Chin. Phys. B, 2025, 34 (**8**): 088501. DOI: 10.1088/1674-1056/add50a
http://cpb.iphy.ac.cn; http://iopscience.iop.org/cpb

What follows is a list of articles you may be interested in

Lewis acid-doped transition metal dichalcogenides for ultraviolet-visible photodetectors

Heng Yang(杨恒), Mingjun Ma(马明军), Yongfeng Pei(裴永峰), Yufan Kang(康雨凡), Jialu Yan(延嘉璐), Dong He(贺栋), Changzhong Jiang(蒋昌忠), Wenqing Li(李文庆), and Xiangheng Xiao(肖湘衡)
Chin. Phys. B, 2024, 33 (**9**): 098501. DOI: 10.1088/1674-1056/ad597f

High responsivity photodetectors based on graphene/WSe_2 heterostructure by photogating effect

Shuping Li(李淑萍), Ting Lei(雷挺), Zhongxing Yan(严仲兴), Yan Wang(王燕), Like Zhang(张黎可), Huayao Tu(涂华垚), Wenhua Shi(时文华), and Zhongming Zeng(曾中明)
Chin. Phys. B, 2024, 33 (**1**): 018501. DOI: 10.1088/1674-1056/acfa84

High performance solar-blind deep ultraviolet photodetectors via *β*-phase $(In_{0.09}Ga_{0.91})_2O_3$ single crystalline film

Bicheng Wang(王必成), Ziying Tang(汤梓荧), Huying Zheng(郑湖颖), Lisheng Wang(王立胜), Yaqi Wang(王亚琪), Runchen Wang(王润晨), Zhiren Qiu(丘志仁), and Hai Zhu(朱海)
Chin. Phys. B, 2023, 32 (**9**): 098508. DOI: 10.1088/1674-1056/acd3e4

Ultra-high photoresponsive photodetector based on ReS_2/SnS_2 heterostructure

Binghui Wang(王冰辉), Yanhui Xing(邢艳辉), Shengyuan Dong(董晟园), Jiahao Li(李嘉豪), Jun Han(韩军), Huayao Tu(涂华垚), Ting Lei(雷挺), Wenxin He(贺雯馨), Baoshun Zhang(张宝顺), and Zhongming Zeng(曾中明)
Chin. Phys. B, 2023, 32 (**9**): 098504. DOI: 10.1088/1674-1056/acd9c0

The growth and expansive applications of amorphous Ga_2O_3

Zhao-Ying Xi(奚昭颖), Li-Li Yang(杨莉莉), Lin-Cong Shu(舒林聪), Mao-Lin Zhang(张茂林), Shan Li(李山), Li Shi(史丽), Zeng Liu(刘增), Yu-Feng Guo(郭宇锋), and Wei-Hua Tang(唐为华)
Chin. Phys. B, 2023, 32 (**8**): 088502. DOI: 10.1088/1674-1056/accf81

Self-powered broadband photodetector based on pyramid-structured Si/TiO_2 heterojunction

Leyao Wu(吴乐瑶), Xinnan Shi(师馨楠), Haibo Fan(范海波), Qiujie Li(李秋洁)†, Peng Hu(胡鹏), and Feng Teng(滕凤)‡

School of Physics, Northwest University, Xi'an 710127, *China*

(Received 31 March 2025; revised manuscript received 28 April 2025; accepted manuscript online 7 May 2025)

Traditional Si-based photoconductive detectors face problems such as low response in the ultraviolet (UV) and infrared regions, high dark current, and low light absorption efficiency, which seriously limit their applications in the field of high-performance wide-spectrum detection. In this study, a self-powered broadband photodetector based on a Si/TiO_2 heterojunction is proposed. The detector has a pyramidal structure. By constructing a pyramidal microstructure on the surface of silicon, the light capture and absorption efficiency is significantly improved, representing a breakthrough in response performance in the visible and near-infrared (NIR) bands. In order to further enhance the photoelectric response in the UV band, a TiO_2 layer was coated on the surface of the silicon pyramid through a simple spin-coating method and annealing process. The introduction of TiO_2 effectively broadened the spectral response range of the photoelectric detector and further improved the light absorption of the device. Meanwhile, due to the built-in electric field formed by the n-TiO_2/p-Si heterojunction, the dark current was effectively reduced, and the responsivity was improved. Experiments showed that the device exhibits high responsivity, high detectivity, and relatively low dark current in the range of 365–1305 nm. Under light at 780 nm, the device's on–off ratio reached 2.7×10^3; its specific detectivity, D^*, was 3.9×10^{11} Jones; and its responsivity reached 0.174 A/W. In addition, this detector does not require the assistance of expensive equipment. Its preparation process is simple and inexpensive, and there is no need for an external power supply, which gives it broad application potential in wearable devices, environmental monitoring, communications, biosensing, and other fields. This study provides a brand-new strategy for the design of new wide-spectrum detectors.

Keywords: photodetector, heterojunction, photoconduction and photovoltaic effects, electronic transport

PACS: 85.60.Gz, 73.40.Lq, 73.50.Pz, 73.50.–h

DOI: 10.1088/1674-1056/add50a **CSTR:** 32038.14.CPB.add50a

1. Introduction

With the exponential growth of information technology and smart devices, optoelectronic detectors have emerged as critical sensing components, playing a pivotal role in diverse fields such as modern communications, environmental monitoring, and advanced imaging systems, among others.[1–3] Conventional optoelectronic detectors predominantly depend on external power sources and are restricted to narrow spectral ranges, such as the ultraviolet (UV), visible, or near-infrared (NIR) regions.[4,5] However, increasingly complex detection tasks — including UV-based ozone layer monitoring and infrared-based greenhouse gas analysis in environmental applications — have driven demand for next-generation detectors with broadband spectral responsivity and self-powered operation. To meet diverse development needs and the trend toward future integrated portable applications, these detectors are becoming a focus of research.[6,7] Such photodetectors can detect signals from UV to NIR spectral ranges. They also operate autonomously by generating photocurrent, reducing reliance on external power sources. This capability decreases system complexity and power consumption, offering significant advantages, particularly in low-power, long-term, and remote monitoring scenarios.[8] To meet the increasing demand for wide-spectrum detectors, researchers have proposed various strategies to extend the spectral response range of detectors, among which the choice of materials is key. In recent years, researchers have made significant efforts to explore materials to meet the demand for wide-spectrum optoelectronic detectors. Traditional semiconductor materials, such as silicon (Si) and gallium arsenide (GaAs), while performing excellently in the visible light range, exhibit relatively weak responses in the UV and infrared ranges, thus limiting their application scope.[9–11] Therefore, the development of novel materials or material composites, particularly those spanning the UV-to-NIR spectrum, has emerged as a pivotal strategy for advancing the functional capabilities of optoelectronic detectors.[12–14] Li *et al.* demonstrated a highly sensitive photodetector based on a graphene/WSe_2 vertical heterostructure where the WSe_2 layer acted as both the light absorption layer and the localized grating layer. The photodetector exhibited ultrahigh responsivity of 3.85×10^4 A/W and an external quantum efficiency of 1.3×10^7%.[15] Fahad *et al.* successfully fabricated a CdTe/Ge/Si photodetector using thermal evaporation and pulsed laser deposition tech-

†Corresponding author. E-mail: liqj@nwu.edu.cn

‡Corresponding author. E-mail: tengfeng@nwu.edu.cn

© 2025 Chinese Physical Society and IOP Publishing Ltd. All rights, including for text and data mining, AI training, and similar technologies, are reserved.

niques. This detector achieved a wide spectral detection range, with a maximum responsivity of 25 A/W and a detectivity of 41×10^{16} Jones.[16] Hassan *et al.* achieved wide spectral detection from 400 nm to 1000 nm by constructing a Co_3O_4/ZnO/Si device. The device demonstrated responsivities of 3.5 A/W at 480 nm and 4.5 A/W at 950 nm, laying the foundation for the design of high-performance metal oxide heterojunction optoelectronic detectors.[17] Song *et al.* used a modified metal-assisted chemical vapor deposition method to grow a high-quality ZnTe and TeO_2 (ZTO) composite material on an n-type silicon substrate. The optoelectronic detector demonstrated a broad spectral light response from the UV region to the NIR region (350–850 nm). Under zero bias voltage and 850 nm illumination, the detector exhibited a high responsivity of 75 mA/W and a detectivity of 1.4×10^{11} cm·Hz$^{1/2}$·W^{-1}. This photodetector integrates third-generation oxide semiconductors with first-generation silicon semiconductors, offering a promising pathway toward integrated multiband detection systems.[18] Concurrently, to achieve self-powering functionality, researchers have investigated photonic-to-electric energy conversion mechanisms, including photovoltaic-based energy harvesters and photocurrent-driven device architectures. Existing approaches, such as photovoltaic thin-film composites,[19–21] quantum dot structures,[22,23] and nanowire arrays,[24,25] have demonstrated broadband spectral sensitivity from the UV region to the NIR region while exhibiting self-powered performance under specific conditions. However, these solutions often involve complex material fabrication processes or expensive raw materials, limiting their scalability and practical implementation.

Among various candidate materials, titanium dioxide (TiO_2) has emerged as a prominent optoelectronic detection material owing to its wide bandgap (~ 3.2 eV), exceptional optical characteristics, and remarkable chemical stability.[26,27] Notably, TiO_2 demonstrates strong UV light absorption while maintaining robust radiation resistance, enabling sustained optoelectronic conversion efficiency even under extreme environmental conditions.[28] However, pure TiO_2 materials often suffer from rapid carrier recombination and inefficient charge separation, significantly constraining their practical performance. To address these limitations, heterostructure engineering through coupling TiO_2 with complementary semiconductors (e.g., Si, NiO, ZnO, and CdS) has proven effective for enhancing optoelectronic detector performance.[29–31] Among these, silicon stands out as particularly advantageous due to its mature fabrication processes, cost-effectiveness, and superior electrical properties, especially within the visible spectrum.[32] However, the light absorption capacity of silicon is weak in the shorter-wavelength UV and longer wavelength infrared light regions, which presents certain limitations in photodetectors with a wide spectral response. Combining silicon with TiO_2 leverages the strengths of both materials, achieving efficient photoelectric conversion across a wide spectral range.[33,34] For instance, TiO_2 exhibits strong UV light responsivity, while silicon demonstrates superior absorption in the visible-to-NIR spectrum, enabling broadband optoelectronic detection. To further enhance device performance, recent research has focused on micro/nanostructural engineering approaches.[35] Among these, pyramid-shaped nanostructures have shown particular promise due to their exceptional light-trapping capabilities, significantly improving absorption efficiency across the UV–visible (UV–vis) spectral range.[36] In addition, the geometric characteristics of pyramidal structures can effectively optimize charge separation and carrier transport, thereby enhancing the electrical performance of the device.[37]

In this study, a TiO_2–silicon (Si) composite material was fabricated with a pyramid-structured design that synergistically enhanced light absorption efficiency and achieved a broad spectral response spanning the UV, visible, and NIR spectral ranges. Its photocurrent-driven operation in a self-powered mode eliminates the requirement for an external power source, thereby synergistically reducing power consumption while enhancing long-term operational stability and device reliability. Compared to other material systems characterized by complex fabrication processes or elevated production costs, the selection of TiO_2 as the primary material synergistically enhances detector performance while retaining a structurally simple and energetically efficient device architecture. Such a novel optoelectronic detector is anticipated to play a pivotal role in diverse future applications, including smart devices, environmental monitoring, and health diagnostics.

2. Experimental details

2.1. Materials

All the chemicals and solvents used in the experiment were of analytical grade and used without any purification. Acetone was provided by Sinopharm Chemical Reagent Co., Ltd. (Shanghai, China). Polyvinylpyrrolidone (PVP, with a molecular weight of ~ 1300000) was purchased from Shanghai Aladdin Biochemical Technology Co., Ltd. (Shanghai, China). Butyl titanate was supplied by Tianjin Damao Chemical Reagent Factory (Tianjin, China). Dimethylformamide (DMF) was obtained from Tianjin Tianli Chemical Reagent Co., Ltd. (Tianjin, China). Glacial acetic acid was purchased from Chengdu Kelong Chemical Co., Ltd. (Chengdu, China). Titanium isopropoxide was supplied by Shanghai Aladdin Biochemical Technology Co., Ltd. (Shanghai, China). Textured Si (100) was purchased from Lanqiao New Energy Technology Co., Ltd. (Xi'an, China).

2.2. Preparation of TiO_2 layer

Before we prepared the surface oxide layer, the silicon wafers were ultrasonically cleaned in acetone, alcohol, and deionized water for 10 min each. The cleaned silicon wafers were dried with a nitrogen gun. Then, 0.5 ml of tetrabutyl titanate, 0.5 ml of DMF, and 1 ml of glacial acetic acid were added to 2.5 ml of absolute ethanol. While stirring the mixture, 0.2 g of PVP (with a molecular weight of approximately 1300000) was added, and the mixed solution was stirred at 95 °C for 20 min to obtain the TiO_2 precursor solution. We used tape to limit the spin-coating area so that two-thirds of the silicon wafer was exposed. During the spin coating process, we transferred 40 µl of the TiO_2 precursor solution to the uncovered area with a pipette. The spin coater was set to run at a speed of 500 rpm for 10 s and then at 2500 rpm for 20 s. The spin-coating process was adopted to conduct spin-coating operations one, three, and five times on the pyramid-structured silicon (Si) substrates. The samples thus obtained were named L1, L3, and L5 in sequence. In addition, P1 refers to the sample prepared after only one spin-coating operation on the flat silicon (Si) substrate. After spin-coating was completed, the samples were transferred to a muffle furnace for annealing. The starting temperature was 30 °C and the heating rate was 3 °C/min. The samples were kept at 400 °C for 120 min and then naturally cooled to room temperature. A drop of silver paste was placed on the surface of the obtained TiO_2 film to form an electrode, and the other electrode was attached to the Si. After further drying, the TiO_2/Si pyramidal photodetectors were finally obtained. A schematic diagram of the device structure is shown in Fig. 1.

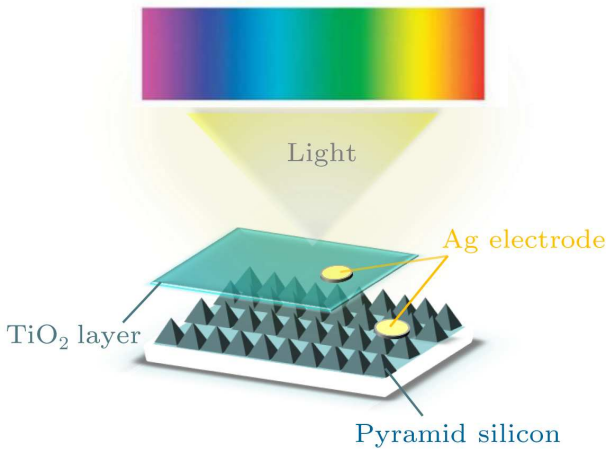


Fig. 1. Schematic diagram of the device structure.

2.3. Characterization

The morphologies and structures of all samples were characterized by scanning electron microscopy (SEM, SU8020, Japan). The materials were characterized using x-ray diffraction (XRD, DX-2700, HaoYuan, China). The composition of the oxide layer was measured by x-ray photoelectron spectroscopy (XPS, Thermo Fisher, ESCALAB Xi^+). UV–vis diffuse reflection spectra (DRS) were measured using a UV-vis spectrophotometer (F-7000, Hitachi, Japan) at room temperature in the wavelength range of 200–1350 nm.

2.4. Photodetection performance measurement

The steady-state electrical performance of the obtained photodetector was measured using a homemade probe station with a Keysight B2901A source meter as an external power supply. Light-emitting diode (LED) lamps with central wavelengths of 365 nm, 515 nm, 635 nm, 780 nm, 880 nm, 1200 nm, and 1305 nm were selected as light sources. A DHC GCI-73 multifunctional precision electronic timer and a DHC GCI-7103 M-B shutter were used to measure the current–time (I–t) curves of the photodetectors.

3. Results and discussion

Figure 2 presents SEM characterization of the textured silicon substrate. As is evident in Figs. 2(a) and 2(b), the surface displays a homogeneous distribution of densely packed pyramid structures. Cross-sectional views (Figs. 2(c) and 2(d)) reveal a well-defined pyramidal morphology with uniform apex angles, confirming the structural regularity of the textured surface. Comparative analysis with planar silicon (Fig. S1) demonstrates that the texturing process introduces significant surface topography modifications, including increased microstructural features and surface defects. These morphological alterations are expected to substantially influence light propagation dynamics at the silicon interface.

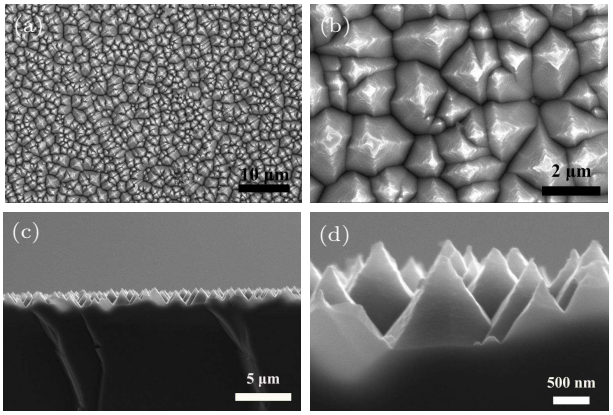


Fig. 2. SEM image of Si texture.

Test results demonstrating the optoelectronic detection performances of flat Si and textured Si are plotted in Fig. 3, which clearly demonstrates the impact of the microstructure on the optoelectronic detection performance. Figure 3(a) shows the dark current of the planar silicon photodetector, which displays good symmetry. Figure 3(b) is an current–voltage (I–V) plot of a flat Si device at 365–880 nm, which exhibits a low on–off ratio in the UV range. Figure 3(c) presents

I–t images of flat Si devices at different wavelengths. Under 880 nm light and a bias of −5 V, the photocurrent reaches a maximum of 5 μA. The photocurrent reaches a maximum of 3 μA at 780 nm, while the photocurrent at 365 nm is low (as shown in Fig. 3(d)), which corresponds to the *I–V* image. The photocurrent at 365 nm and a bias of −5 V is only 1.6 μA. Figure 3(e) shows the photoelectric detection performance of textured Si. Figure 3(a) illustrates the dark current of the textured Si device, with the lowest dark current being 5.03×10^{-8} A. Figure 3(f) is an *I–V* plot of the textured Si. It can be seen that good symmetry is exhibited over the entire spectral range. This symmetry is attributed to the uniformity of the Ag electrodes and the ohmic contact between the electrodes and the Si. Figure 3(g) presents an *I–t* plot of the textured Si. Under illumination by 780 nm light and a bias voltage of −5 V, the photocurrent is approximately 8 μA. Good photoresponse and fast response times are observed over the entire spectral range. Figure 3(h) is an enlarged *I–t* plot of the area within the dotted line in Fig. 3(g) under illumination by light at 365 nm. Under 365 nm illumination with a −5 V applied bias, the device exhibits a relatively low photocurrent of ∼ 0.25 μA. Current–voltage characteristics measured under illumination at 1200 nm and 1305 nm (Fig. S2) reveal that both textured and planar silicon substrates maintain low dark-current levels in this spectral regime. Notably, the photocurrent response remains indistinguishable from the dark current, indicating negligible photoresponse at these wavelengths. This behavior arises from silicon's inherently weak absorption in the NIR spectral region.

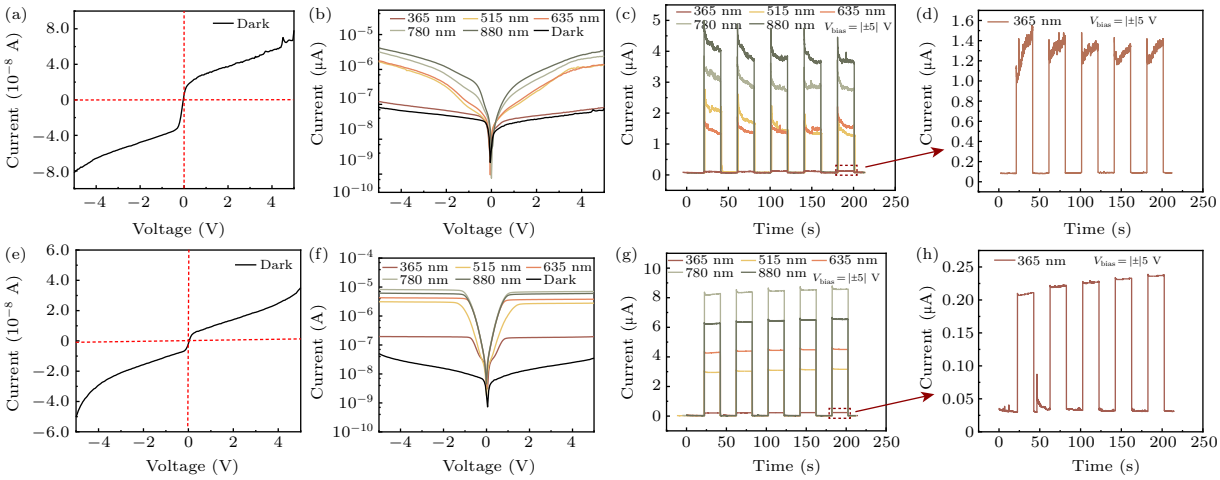


Fig. 3. Photoelectric detection performance of photodetectors based on flat Si (a)–(d) and textured Si (e)–(h). (a) and (e) Dark currents; (b) and (f) current–voltage curves; (c) and (g) current–time curves; (d), (h) current–time curves at 365 nm.

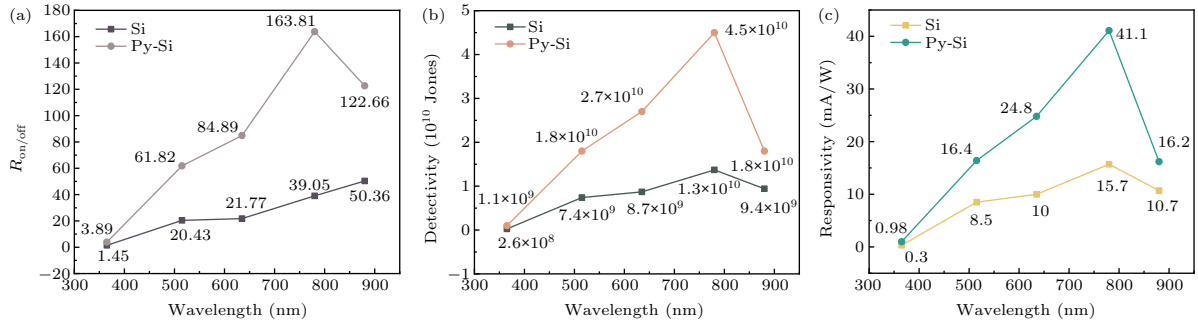


Fig. 4. Performance diagrams for textured Si and flat Si. (a) $R_{on/off}$, (b) detectivity, (c) responsivity.

Three key parameters characterize photodetector performance: responsivity, on–off ratio, and detectivity. Responsivity quantifies the detector's photoelectric conversion efficiency, while the on–off ratio measures the contrast between illuminated and dark currents, reflecting the device's sensitivity and optical switching capability. Detectivity represents the detector's signal-to-noise performance. Figure 4 compares these parameters for both textured and planar devices. Notably, at a bias of −5 V (Fig. 4(a)), the textured device demonstrates significant enhancement across all spectral bands, with the on–off ratio increasing by 268% (from 1.45 to 3.89) at 365 nm. The enhancement in on–off ratio is particularly remarkable at 880 nm, exhibiting a 420% improvement over planar silicon and achieving a maximum value of ∼ 163.81. Figure 4(b) reflects the change in detectivity before and after etching, under a bias of −5 V. The textured device demonstrates substantially improved detectivity, reaching 4.5×10^{10} Jones under illumination at 880 nm — a 4.5-fold enhancement over the pla-

nar device's 1.3×10^{10} Jones. Similar improvements are observed across other wavelengths: UV (365 nm) detectivity increases from 2.6×10^{8} Jones to 1.1×10^{9} Jones, while visible-range (515 nm) performance improves from 7.4×10^{9} Jones to 1.8×10^{10} Jones. Figure 4(c) shows the responsivity spectrum, which follows the same trend as the on–off ratio and detectivity. The responsivity also exhibits significant improvements across the entire wavelength range. Under a bias of −5 V, the textured device exhibits substantial responsivity improvements of 326%, 192%, 248%, 261%, and 151% across the 365–880 nm spectral range. These comprehensive performance enhancements confirm the effectiveness of surface texturing in boosting the detector's photoelectric conversion efficiency.

To systematically evaluate the light-trapping effects of the pyramidal morphology, UV–vis diffuse reflectance spectroscopy was used to examine both the planar and textured silicon (denoted by Py-Si) samples (Fig. S3). The Py-Si demonstrates substantially enhanced absorption across the entire measured spectrum, particularly in the visible region, while maintaining relatively lower absorption beyond 1000 nm. This broadband enhancement originates from multiple light reflections within the pyramidal surface architecture, which effectively increase the optical path length while simultaneously suppressing surface reflectance. The combined effect of these mechanisms promotes more efficient photon capture and absorption across multiple wavelengths.

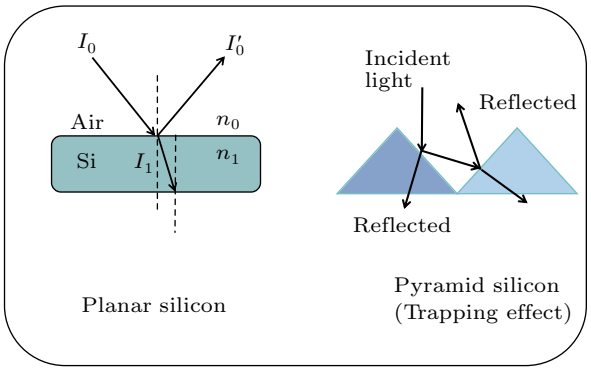


Fig. 5. Schematic diagram showing the propagation paths of light on flat silicon and pyramidal silicon.

Figure 5 illustrates the distinct light propagation mechanisms in planar surfaces versus Py-Si surfaces. In flat silicon, photons are easily reflected and escape after striking the surface. However, the surface structure of textured silicon effectively increases light reflection and scattering, allowing more photons to penetrate deeper into the material, reducing light loss and thereby enhancing the detector's gain and signal strength. The micrometer-scale pyramidal structures created by surface texturing provide three key advantages: first, they increase the effective absorption area through surface roughness. Second, they promote omnidirectional light coupling by accepting photons across a wider angular range (beyond normal incidence). Third, they function as an integrated antireflective mechanism through geometrically induced light scattering. These combined effects lead to superior photoconductive gain and angular response stability in Py-Si photodetectors compared to their planar counterparts.

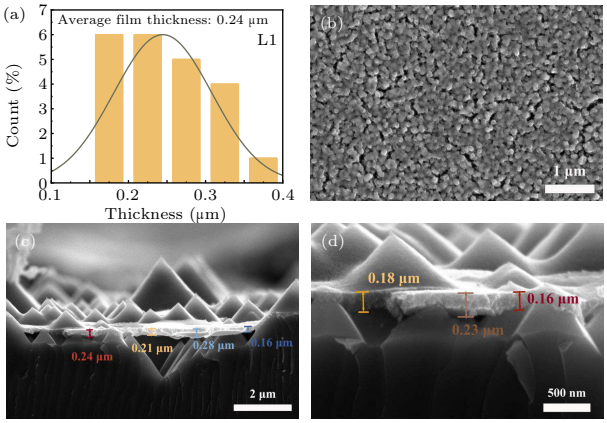


Fig. 6. (a) Statistical histogram of thickness. (b) SEM image and (c)–(d) SEM cross-sectional characterization of the device after it was spin-coated with a layer of TiO_2.

After texturing, the performance of the Si photodetectors shows significant improvement compared to the initial Si photodetectors. However, they still exhibit low photoresponse in the UV range (365 nm). To enhance UV detection capabilities, a TiO_2 thin film was deposited onto the pyramidal silicon substrates via spin-coating. Figure 6 presents the cross-sectional SEM characterization of the resulting heterostructure, while Fig. 6(a) quantitatively analyzes the TiO_2 layer thickness distribution. The L1 sample exhibits a thickness range of 160–380 nm (mean: 240 nm), which provides optimal UV absorption given TiO_2's high extinction coefficient in this spectral region. This conformal coating thickness ensures efficient photon capture while maintaining the underlying pyramidal light-trapping geometry. Figure 6(b) shows an SEM planar view of the TiO_2 layer, revealing a dense and uniformly distributed nanoparticle morphology. Figures 6(c) and 6(d) display SEM images of the device with a spin-coated single layer of TiO_2 at different magnifications. The lower-magnification image (Fig. 6(c), 2 μm scale bar) clearly preserves the underlying pyramidal topography. Notably, the interfacial architecture between the TiO_2 film and the silicon pyramids forms optical microcavities that promote multiple light reflections, thereby enhancing photon absorption through extended optical path lengths. Figure 6(d) displays a high-magnification SEM image (500 nm scale bar) confirming the exceptionally uniform thickness of the TiO_2 coating. To illustrate the impact of different oxide layer thicknesses on device performance, cross-sectional images of the TiO_2/Si pyramid devices after three and five rounds of spin-coating are shown in Fig. S4. Quantitative analysis reveals: (1) the L3 sample (three coatings) shows

a thickness distribution of 300–600 nm (mean: 470 nm), representing a 230 nm increase over L1; (2) the L5 sample (five coatings) exhibits a tightly controlled thickness range of 560–600 nm (mean: 540 nm, +300 nm vs. L1). Cross-sectional imaging (Fig. S4(b)) demonstrates that all coatings maintain excellent conformality and surface planarity despite increasing thickness.

Figure 7 presents the XRD pattern of the deposited TiO_2 film with reference to the standard anatase diffraction pattern (PDF#21-1272). The spectrum exhibits characteristic TiO_2 peaks at 25.3° (101) and 38.2° (112), confirming the formation of the crystalline anatase phase. The broad feature centered at 29° originates from the underlying polycrystalline silicon substrate. Due to the thin TiO_2 layer, light passing through the TiO_2 layer primarily interacts with the silicon surface, thus reflecting some surface information. Polycrystalline silicon and amorphous silicon exhibit differences in the shape and intensity of their diffraction peaks, as evidenced by peak broadening characteristic of multioriented grains. This peak broadening contrasts sharply with the featureless background expected for amorphous silicon, thereby confirming the polycrystalline nature of the substrate. In the XRD spectrum, polycrystalline silicon typically exhibits broader diffraction peaks due to the presence of grains with different orientations, leading to peak broadening. In contrast, amorphous silicon usually lacks distinct diffraction peaks. This determines the presence of polycrystalline silicon. The peak around 38° corresponds to the (112) plane of TiO_2.

The presence of TiO_2 was further confirmed by measuring the XPS spectra. The spectrum of the TiO_2 layer on silicon is shown in Fig. 8. Figure 8(a) presents the full spectrum of TiO_2, where characteristic peaks corresponding to Ti 2p, O 1s, C 1s, and Si 2p are observed. The C 1s signal may originate from adsorbed organic materials or carbon dioxide. From Fig. 8(b), it can be seen that the peaks at 99.5 eV and 101.5 eV correspond to Si $2p_{3/2}$ and Si $2p_{1/2}$ orbitals, respectively.[38] Figure 8(c) shows the O 1s signal, where the O 1s spectrum exhibits a prominent peak around 530 eV, attributed to the oxygen in the TiO_2 lattice.[39] In the Ti 2p spectrum shown in Fig. 8(d), two peaks appear at approximately 458.5 eV and 464.2 eV, corresponding to the Ti $2p_{3/2}$ and Ti $2p_{1/2}$ orbitals, respectively. This indicates that titanium is present in the Ti oxidation state, which is a typical feature of TiO_2.[40] These characteristics confirm the chemical composition and surface properties of the TiO_2 material.

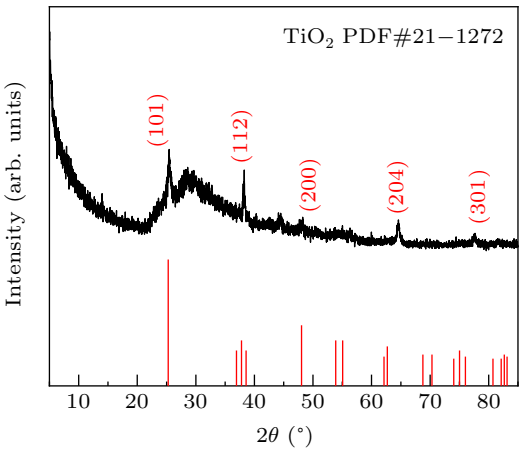


Fig. 7. XRD image of the deposited TiO_2.

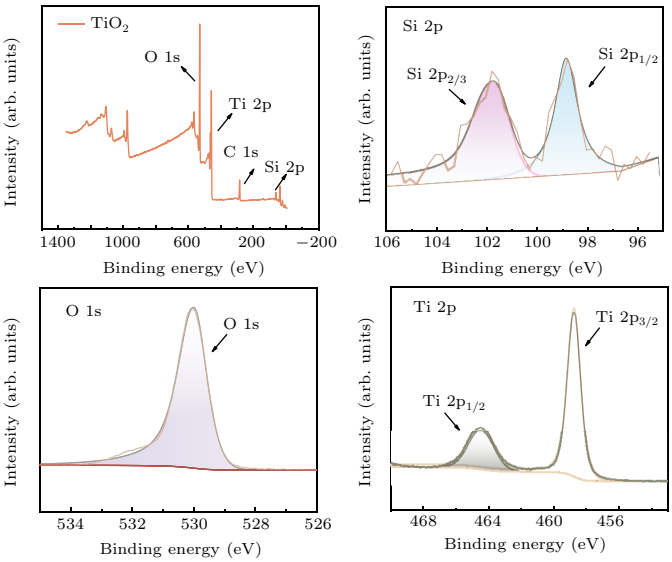


Fig. 8. XPS spectra of the TiO_2 layer on the silicon wafer: (a) survey spectra; fine spectra of (b) Si 2p, (c) O 1s, and (d) Ti 2p.

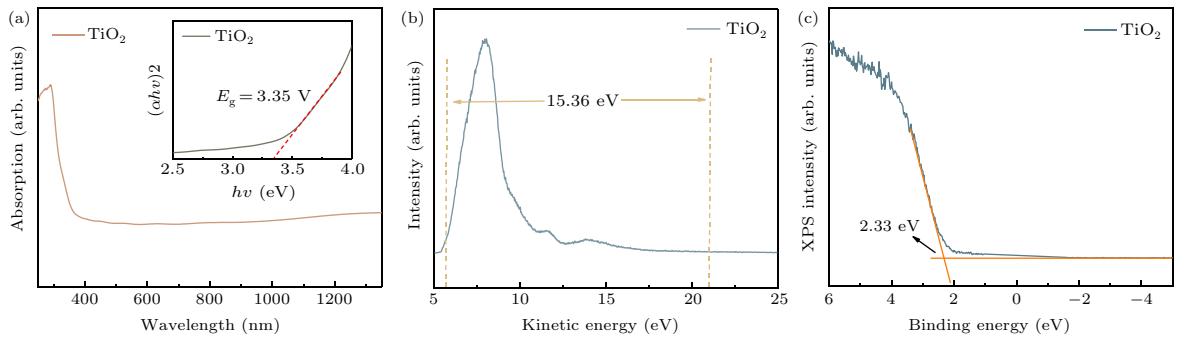


Fig. 9. Absorption and UPS spectra of TiO_2: (a) UV–vis DRS spectra of TiO_2 (insert shows the corresponding Tauc plot); (b) UV photoelectron spectroscopy (UPS); (c) XPS valence band spectrum.

The optical and electronic properties of TiO_2 were systematically characterized using complementary spectroscopic techniques. UV–vis diffuse reflectance spectroscopy (Fig. 9(a)) reveals a sharp absorption onset at 380 nm, corresponding to a direct bandgap of 3.35 eV as determined from Tauc plot analysis. This demonstrates strong UV absorption ($<$ 380nm) due to band-to-band transitions while maintaining high transparency in the visible region ($>$ 400 nm). UV photoelectron spectroscopy (UPS, Fig. 9(b)) establishes the absolute energy alignment, showing a secondary electron cutoff at 5.86 eV relative to the vacuum level. XPS valence band analysis (Fig. 9(c)) further determines that the valence band maximum lies 2.33 eV below the Fermi level. This electronic structure configuration, with the Fermi level positioned near the conduction band, conclusively confirms the n-type semiconductor character of the deposited TiO_2 films.

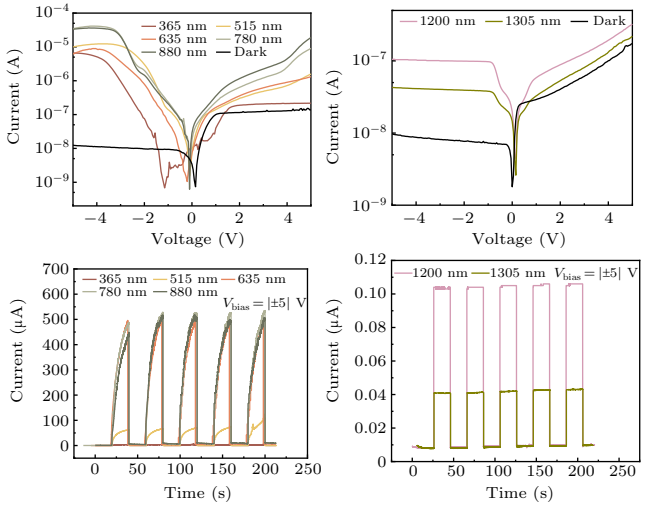


Fig. 10. Photoelectric detection performance of a TiO_2/Si pyramid device with a thickness of 0.24 μm: (a) current–voltage curves at 365–880 nm, (b) current–voltage curves at 1200–1305 nm, (c) current–time curves at 365–880 nm, (d) current time curves at 1200–1305 nm.

Figure 10 illustrates the optoelectronic performance of the device after spin-coating one layer of TiO_2. From Fig. 10(a), it can be seen that the on–off ratio at 365 nm shows significant improvement, with the photocurrent reaching a maximum of 3.47×10^{-5} A. The formation of a heterojunction between the TiO_2 and the Si leads to a reduction in dark current, which reaches a minimum value of 1.25×10^{-8} A. The TiO_2/Si pyramid device exhibits a broader response range. The optoelectronic response characteristics were systematically evaluated under infrared and visible illumination. Figure 10(b) presents the current–voltage characteristics in the 1200–1305 nm spectral range, where the observed photocurrent originates primarily from interfacial effects at the TiO_2/Si heterojunction. Notably, the on–off ratio exhibits an inverse relationship with increasing infrared wavelength, suggesting wavelength-dependent carrier generation mechanisms. Time-resolved photoresponse analysis (Fig. 10(c)) at a bias of −5 V confirms stable operation across the 365–880 nm spectrum. In particular, under illumination at 780 nm, the device achieves a peak photocurrent of 550 μA with rapid switching characteristics (τ_r = 12 s, τ_d = 20 ms). The asymmetric response times indicate distinct charge trapping and release dynamics within the heterostructure. Figure 10(d) presents the temporal photoresponse characteristics under NIR illumination (1200–1305 nm) at a bias of −5 V. The device exhibits significantly lower photocurrent generation in this spectral regime, reaching maximum values of only 0.1 μA at 1200 nm and 0.04 μA at 1305 nm. This attenuated response is consistent with the reduced absorption coefficient of silicon at longer wavelengths and confirms the previously observed wavelength-dependent performance trends.

The photoelectric detection performance of the device after spin coating three layers of TiO_2 is shown in Fig. S5. From Fig. S5(a), it can be observed that as the TiO_2 layer thickness increases, the on–off ratio decreases. Under a bias of −5 V and 880 nm illumination, the photocurrent reaches 2.08×10^{-5} A, which is three orders of magnitude higher than the dark current (3×10^{-8} A). The low dark current is attributed to the effects of the p–n junction at the TiO_2/Si pyramid interface.

Electrical characterization under NIR illumination (Fig. S5(b)) reveals limited photoresponse in the 1200–1305 nm range, with photocurrent-to-dark-current ratios below one order of magnitude. From the current–time curve in Fig. S5(c), it can be seen that under a bias of −5 V and illumination in the 365–880 nm range, there is a clear photoresponse. After five cycles, the photocurrent shows almost no decay, indicating that the device has good stability. The attenuated NIR response is further quantified in Fig. S5(d), which shows maximum photocurrents of 0.11 μA (1200 nm) and 0.06 μA (1305 nm) under a bias of −5 V. This wavelength-dependent performance aligns with the expected absorption characteristics of the TiO_2/Si heterostructure.

The optoelectronic performance of the device after spin-coating five layers of TiO_2 is shown in Fig. S6. From Fig. S6(a), it can be seen that, compared to the L1 device, there is no significant change in the dark current, but the photocurrent has decreased. Device performance analysis reveals two notable characteristics: (i) the on–off ratio under 1305 nm illumination at a bias of −5 V shows a significant reduction compared to the on–off ratio at shorter wavelengths (Fig. S6(b)), and (ii) the time-dependent photoresponse in the 365–880 nm range (Fig. S6(c)) demonstrates constrained current generation, with photocurrent values ranging from 0.5 μA to 5 μA. Figure S6(d) presents the *I*–*t* curve under a bias of −5 V and illumination at 1200–1305 nm. The photocurrent is relatively small, but the device shows fast rise and fall times, indicating a quick response.

The on–off ratio, responsivity, and detectivity of the

TiO_2/Si pyramid device (L1) are shown in Fig. 11. Under 780 nm illumination and a bias of −5 V, the device exhibits exceptional performance metrics, including an on–off ratio of 2.76×10^3, a detectivity of 3.90×10^{11} Jones, and a responsivity of 0.17 A/W. To better compare the performance across different thicknesses (L1, L2, L3), we calculated the on–off ratio, responsivity, and detectivity for each device and plotted them in Fig. S7. Figure S7 illustrates the impact of TiO_2 layer thickness on device performance. From the on/off ratio (Fig. S7(a)), detectivity (Fig. S7(b)), and responsivity results (Fig. S7(c)), it is evident that as the TiO_2 layer thickness increases, the device performance gradually decreases. Notably, the device maintains consistent performance characteristics at NIR wavelengths (1200–1305 nm), with all key figures of merit showing negligible dependence on TiO_2 layer thickness. This thickness-independent behavior suggests that the photoresponse mechanism in this spectral regime is dominated by interfacial phenomena rather than bulk material properties.

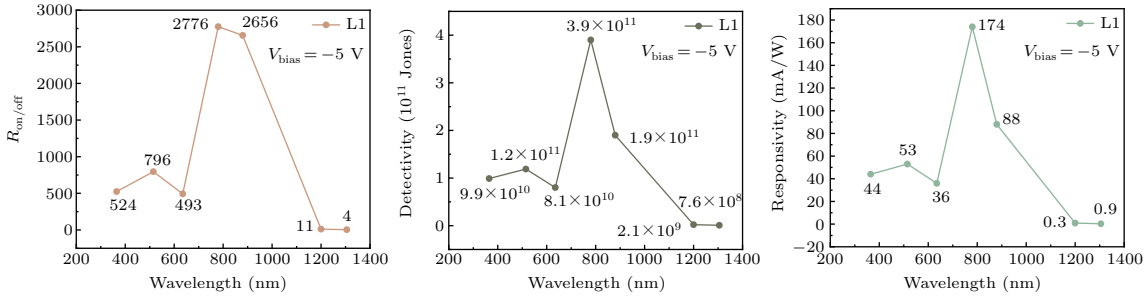


Fig. 11. The performance characteristics of the L1 device under a bias of −5 V: (a) $R_{on/off}$, (b) detectivity, (c) responsivity.

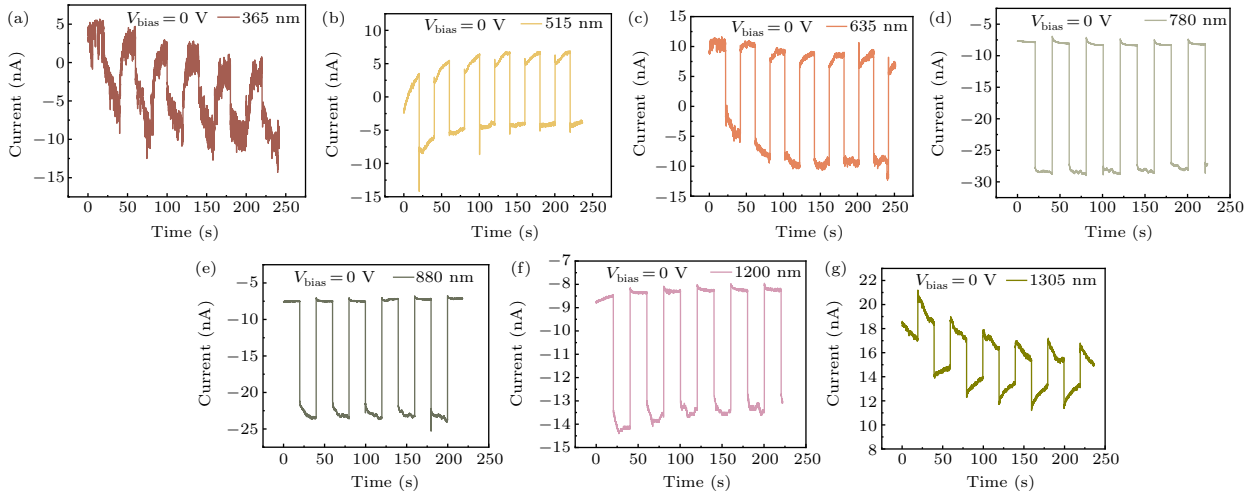


Fig. 12. Photoelectric detection performances of the L1 device at 0 V: (a)–(g) 365–1305 nm.

Compared with the original flat silicon device, under a voltage bias of −5 V, the L1 device yields significant improvements in the on–off ratio, detectivity, and responsivity. Furthermore, this device demonstrates self-powered functionality, operating independently of an external power source. The optoelectronic performance test results for the L1 device at 0 V are depicted in Fig. 12. It is evident that the device showcases distinct self-powered characteristics within the 365–1305 nm wavelength spectrum. The built-in electric field generated at the Si/TiO_2 interface efficiently separates photogenerated electrons and holes, allowing the device to produce photocurrent in the absence of an applied external voltage. Under illumination at 780 nm and a bias of 0 V, the maximum photocurrent reaches 30 nA. To better present the detection performance of the L1 device at 0 V, the detectivity and responsivity of the device are shown in Fig. 13. It can be observed that at 635 nm and a bias of 0 V, the detectivity is 2.8×10^9 Jones, and the responsivity is 0.114 mA/W. This indicates that the device exhibits good self-powering characteristics.

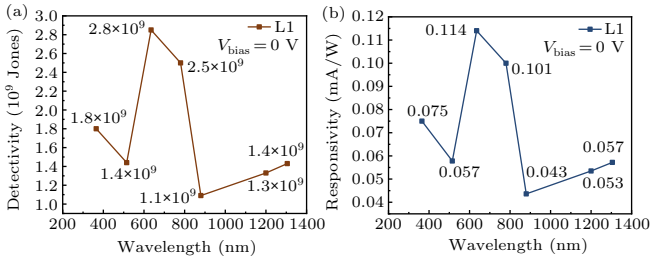


Fig. 13. Performances of the TiO_2/Si pyramid device at 0 V: (a) detectivity, (b) responsivity.

The creation of a distinctive reflective cavity structure between the pyramidal Si and TiO_2 is likely the primary factor contributing to the enhancement of the device's performance.

In light of this, UV–vis diffuse reflectance spectroscopy measurements were carried out on the pyramidal Si device (Py-Si) and the device with a deposited TiO_2 layer (TiO_2/Si pyramid), and the findings are presented in Fig. 14. The introduction of TiO_2 further enhances light absorption in the wavelength range of 350–880 nm, mainly due to the multiple reflections of the incident light in the reflective cavity structure. After being reflected multiple times, the light is absorbed by the materials, which significantly improves their light absorption.

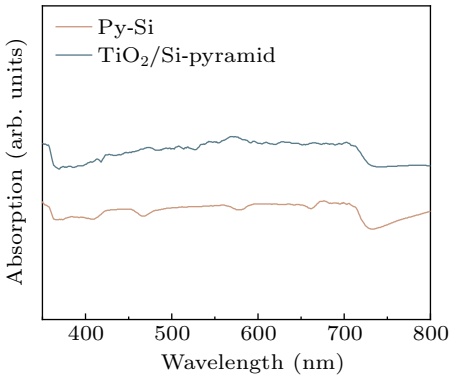


Fig. 14. UV–vis diffuse reflection spectra of Py-Si and the TiO_2/Si pyramid.

To further validate the effect of the formed reflective cavity structure on the device's performance, a TiO_2/Si flat device (designated by P1) was fabricated by spin-coating a TiO_2 thin film onto flat Si. The performance characteristics of this device are illustrated in Fig. S8. By comparing this with the pyramidal Si device, it can be further demonstrated that adding a pyramidal structure to Si enhances the device performance. From Fig. S8, it can be observed that the substrate morphology significantly impacts the device performance. Compared to L1, the P1 device exhibits a photocurrent that is an order of magnitude lower. From Fig. S8(c), it can be seen that under a bias of −5 V, the maximum photocurrent is 30 μA. The self-powered photodetection performance of the device at 0 V is depicted in Fig. S9. As is evident from the figure, device P1 demonstrates a notable pyroelectric effect. The generation of pyroelectric current upon its illumination by light is attributed to the rapid temperature fluctuations in the surrounding environment, which trigger polarization changes within the material. When the light is switched on, the temperature of the material rises, leading to an increase in the internal dipole moment. Consequently, positive charges move outward, and negative charges move inward, giving rise to a positive current. Conversely, when the light is turned off, the temperature of the material drops, causing a decrease in the dipole moment. This results in the outward movement of negative charges and the inward movement of positive charges, generating a negative current. To highlight the performance disparities of devices with different substrates (L1 and P1), the on–off ratio, detectivity, and responsivity values of the two devices are illustrated in Fig. S10. Upon comparison, it is evident that the performance of the L1 device is markedly superior to that of the P1 device. Under a bias voltage of −5 V and illumination at 780 nm, the on–off ratio, detectivity, and responsivity of the L1 device are increased by 295%, 174%, and 216%, respectively, compared to those of the P1 device. This suggests that the presence of the reflective cavity structure enhances the light absorption rate of the materials, thereby improving device performance.

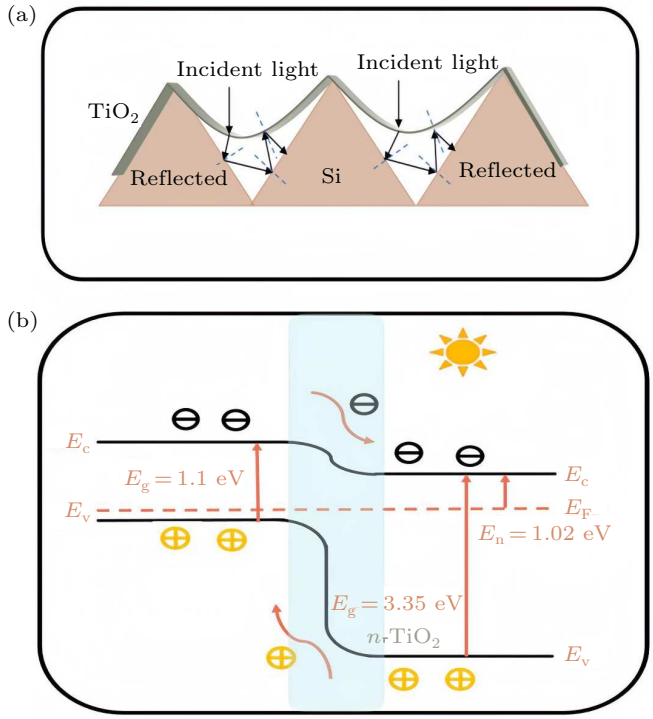


Fig. 15. Schematic diagram showing the operating principle of a TiO_2/Si pyramid device.

Figure 15 illustrates the working principle of this photodetector. The high performance of the TiO_2/Si pyramid device can be attributed to two main factors. First, it is the result of the formation of a special reflective cavity structure. As illustrated in Fig. 15(a), which is a schematic representation of the light propagation pathway within the materials, it is evident that upon depositing a TiO_2 layer on the surface of the pyramid-structured silicon, a reflective cavity is established between the TiO_2 and the Si. The incident light undergoes multiple reflections within the reflective cavity and ultimately penetrates both the Si and the TiO_2. This prolonged optical path significantly enhances light absorption efficiency, thereby contributing to the generation of a high photocurrent in the TiO_2/Si pyramid device. Another factor contributing to the enhanced performance is the formation of a p–n junction between the Si and the TiO_2. As illustrated in Fig. 15(b), when n-type TiO_2 interfaces with p-type Si, the disparity in their Fermi levels induces electron diffusion from the TiO_2 to the Si and hole diffusion from the Si to the TiO_2. This carrier redistribution establishes a charge imbalance at the interface, generating a built-in electric field (depletion region). Under illu-

mination, photons excite electron–hole pairs in both the Si and the TiO_2. The built-in electric field efficiently separates these photogenerated carriers: electrons migrate toward the TiO_2, while holes accumulate in the Si, thereby generating a photocurrent and enabling photodetection. In the absence of light, electrons on the TiO_2 side encounter a high potential barrier that impedes their migration across the p–n junction to the Si side. This barrier effect significantly suppresses carrier transport through the junction, thereby reducing the dark current in the TiO_2/Si pyramid device. Table 1 compares the performance parameters of photodetectors with various heterojunction configurations. The data indicate that the TiO_2/Si pyramid photodetector achieves high-performance, broad-spectrum detection under bias conditions of both −5 V and 0 V.

Table 1. Comparison of the performance parameters of different heterojunction photodetectors.

Photodetector	Wavelength (nm)	R_{max} (mA/W)	D^*_{max} (Jones)	t_{rise}/t_{fall} (s)	Bias (V)	Ref.
TiO_2/pyramidal Si	365–1305	174	3.9×10^{11}	12/0.02	−5	This
TiO_2/pyramidal Si	365–1305	0.144	2.8×10^{9}	< 20 ms	0	work
n-TiO_2/p-Si	365	32.14	0.77×10^{9}	–	8	[41]
graphene/NiO/n-Si	350–800	150	1.78×10^{11}	< 0.8	−5	[42]
p-NiO/n-Si	365	0.160	–	1.53/0.7	−5	[43]
ZnO/TiO_2/Si	365	107	6.75×10^{8}	0.19/0.24	4	[44]
TiO_2 NPs/n–Si	350	45	1.91×10^{12}	–	−3	[45]
TiO_2/n-Si	200–800	13	6.76×10^{7}	–	−5	[46]
Au TF/TiO_2/n-Si	200–800	185	3×10^{9}	–	−5	[46]
TiO_2/ n-Si(111)	300–600	10	–	–	−2	[47]
NiO/n-Si	365	13	1.03×10^{11}	< 80 ms	0	[48]
TiO_2/Si	365	2.04 A/W	2.18×10^{8}	0.73/0.69	−2	[49]

After decades of optimization, silicon-based photodetectors have achieved remarkable maturity in both performance and manufacturing scalability. Some commercial devices (e.g., the Hamamatsu S1223 series and the Thorlabs PDA36A) demonstrate outstanding responsivity (0.4–0.7 A/W in the visible spectrum) and near-ideal quantum efficiency (>80% at 400–900 nm). p–intrinsic–n (PIN) photodiodes and avalanche photodiodes (e.g., the Excelitas C30659) achieve subnanosecond response times, while the First Sensor BPX65 exhibits low noise with dark currents below 1 nA at room temperature. Though commercial Si detectors excel in performance, they rely on complex processes (e.g., high-temperature epitaxy) for their manufacture. Although any single characteristic of the devices proposed in this study falls short of the aforementioned commercial counterparts, these devices achieve a balance of wide spectral detection without degrading visible-light performance, low dark currents, and a simplified fabrication process. This breakthrough fills a long-standing technological gap in low-cost broad-spectrum detection, offering solutions for applications ranging from UV sterilization monitoring to short-wave infrared (SWIR) spectral analysis.

4. Conclusion

In this work, TiO_2/Si pyramid devices were obtained by covering pyramidal-structured Si with a TiO_2 layer through a simple annealing technique. These devices demonstrated a broad detection range spanning 365 nm to 1305 nm. Additionally, the effects of TiO_2 layers with varying thicknesses and Si substrates with distinct structural configurations on device performance were systematically investigated. The results revealed that the TiO_2/Si pyramid device with a single spin-coated layer exhibited optimal detection performance. Under a bias of −5 V and 780 nm illumination, the device achieved an on–off ratio of 2.76×10^3, a detectivity of 3.90×10^{11} Jones, and a responsivity of 0.174 A/W. At a bias of 0 V with 635 nm illumination, it achieved a detectivity of 2.8×10^9 Jones and a responsivity of 0.114 mA/W. This enhanced performance is attributed to the unique reflective cavity structure formed at the Si–TiO_2 interface and the interfacial effects arising from material contact, which collectively enhance light absorption and detection capabilities. This work presents a novel strategy for developing portable, broadband, self-powered photodetectors.

Acknowledgments

Project supported by the National Natural Science Foundation of China (Grant Nos. 51902255 and 51803168), the Natural Science Foundation of Shaanxi Province (Grant No. 2023-JC-YB-015), the Shaanxi Province Key Research and Development Projects (Grant No. 2022GY-356), and the Shaanxi Universities' Youth Innovation Team (Grant No. 23JP174).

References

[1] Lian X, Luo L, Dong M, Miao Z, Qi X, Cai Z and Wang L 2024 *J. Mater. Sci.* **59** 21581

[2] Tang H, Lu D, Zhou Q, Luo S, Huang K, Li Z, Qi X and Zhong J 2022 *Appl. Surf. Sci.* **571** 151335

[3] Zou J, Zhang S and Tang X 2024 *Photonics* **11** 1014

[4] Vu T K O, Tran M T, Xuan Tu N, Thi Thanh Bao N, Thi Khanh Van N, Van Thanh H and Kim E K 2024 *Mater. Sci. Semicond. Process.* **181** 108664

[5] Wang H C, Lin Y, Liu X, Deng X, Ben J, Yu W, Zhu D and Liu X 2023 *Chin. Phys. B* **32** 018504
[6] Zeng Z, Wang D, Fang X, Zhao C, Zhang B, Liu D, Chen T, Pan J, Liu S, Liu G, Liu T, Jin H, Jiao S, Zhao L and Wang J 2023 *Mater. Today Nano* **23** 100372
[7] Gao W, Zheng Z, Huang L, Yao J, Zhao Y, Xiao Y and Li J 2019 *ACS Appl. Mater. Interfaces* **11** 40222
[8] Ban G, Song J, Wang Z, Zhao X, Li Y, Yang J, Ye C, Teng F, Hu P and Fan H 2024 *Surf. Interfaces* **55** 105319
[9] Wu L, Zhang M, Shi X, Hu P, Yu H and Teng F 2024 *IEEE Sens. J.* **24** 20476
[10] Li X, Yu X, Zeng H, Boras G, Shen K, Zhang Y, Wu J, Choy K L and Liu H 2021 *Appl. Phys. Lett.* **119** 53105
[11] Zhao Z, Zou C, Zhou E, Liu Q, Chen K, Wang X, He L, Gao F and Li S 2023 *Surf. Interfaces* **39** 102909
[12] Xiao L, Liu Z and Feng W 2023 *Opt. Mater.* **137** 113512
[13] Wang S, Lv Y, Trigub M V and Yang X 2025 *J. Alloys Compd.* **1010** 177627
[14] Che M, Li Y, Wang B, Yuan J, Qi L, Zou Y, Liu M, Zhao X, Shi Y, Tan F, Feng Y, Li D and Li S 2024 *ACS Photonics* **11** 1693
[15] Li S, Ting L, Zhongxing Y, Yan W, Like Z, Huayao T, Wenhua S and Zhongming Z 2024 *Chin. Phys. B* **33** 018501
[16] Fahad O A, Ramizy A and Al-Rawi B K 2024 *J. Mater. Sci.: Mater. Electron.* **35** 1822
[17] Hassan A I, Hammood I H and Addie A J 2024 *Opt. Mater.* **148** 114974
[18] Song Z, Liu Y, Wang Q, Yuan S, Yang Y, Sun X, Xin Y, Liu M and Xia Z 2018 *J. Mater. Sci.* **53** 7562
[19] Swain AB, Rath M, Biswas PP, Rao MSR and Murugavel P 2019 *APL Materials* **7** 011106
[20] Wu J, Shi Z, Bai Z, Peng T and Luo B 2024 *Ceram. Int.* **50** 16679
[21] Binghui W, Yanhui X, Shengyuan D, Jiahao L, Jun H, Huayao T, Ting L, Wenxin H, Baoshun Z and Zhongming Z 2023 *Chin. Phys. B* **32** 098504
[22] Kim S H, Lee D, Moon S, Choi J H, Kim D, Kim J and Baek S W 2023 *Adv. Funct. Mater.* **33** 2303778
[23] Wu H, Wu C, Guo C, Hu J, Guo D and He S 2024 *Small* **23** 2312127
[24] Yang Z, Ma S, Shi Y, Hao X, Shang L, Han B, Qiu B and Xu B 2024 *Opt. Mater.* **150** 115183
[25] Wang N, Liu X, Jiang D, Zhao M, Wang C, Zhang X and Ding S 2024 *Cryst. Growth Des.* **24** 4781
[26] Shehu Y, Abbas A M A, Ahmed N M, Aslam S, Samsuri S A M and Loh W M E 2025 *Optik* **321** 172188
[27] Li Z, Li Z, Zuo C and Fang X 2022 *Adv. Mater.* **34** 2109083
[28] Park C, Elmughrabi A, Melis A, Kim S, Cho S and Yeom J Y 2024 *Opt. Mater.* **157** 116165
[29] Yang D, Du F, Ren Y, Kang T, Hu P, Teng F and Fan H 2021 *J. Mater. Chem. C* **9** 14146
[30] Yin Z, Shan Y, Yu M, Yang L, Song J, Hu P and Teng F M 2022 *Mater. Sci. Semicond. Process.* **148** 106813
[31] Nallabala N K R, Kaleemulla S, Reddy M R, El-marghany A, Ravi N, Sambasivam S, Sekhar M C, Rosaiah P, Kushvaha S S, Kalaivani V, Shankar M V and Reddy V R M 2024 *Silicon* **16** 2815
[32] Ratnesh R K, Singh M K and Singh J 2024 *J. Mater. Sci.: Mater. Electron.* **35** 756
[33] Rodríguez D F and Perillo P M 2023 *Opt. Mater.* **135** 113315
[34] Cao F, Liao Q, Deng K, Chen L, Li L and Zhang Y 2018 *Nano Res.* **11** 1722
[35] Zhou H, Yang G, Ren D, Huang J, Gao Z, Duan J and Wang H 2022 *Adv. Opt. Mater.* **10** 2201270
[36] Chu L, Zhou X, Xu C, Zhu S, Wu W, Wu R and Zhou S 2024 *Ceram. Int.* **51** 9030
[37] Pei Z, Hu H, Li S and Ye C 2017 *Langmuir* **33** 3569
[38] Cerofolini GF, Galati C and Renna L 2003 *Surface and Interface Analysis* **35** 968
[39] Ji T, Liu Q, Zou R, Zhang Y, Wang L, Sang L, Liao M and Hu J 2017 *J. Mater. Chem. C* **5** 12848
[40] Chen N, Li Y, Deng D, Liu X, Xing X, Xiao X and Wang Y 2017 *Sens. Actuators B: Chem.* **238** 491
[41] Agrohiya S, Kumar V, Rawal I, Dahiya S, Goyal P K, Kumar V and Punia R 2022 *Silicon* **14** 11891
[42] Pandit B, Parida B, Jang H S and Heo K 2024 *Nanomaterials* **14** 551
[43] Al-Hardan N H, Ahmed N M, Almessiere M A and Aziz A A 2020 *Materials Research Express* **6** 126332
[44] Elzawiei Y S M, Abdulhameed A, Hashim M R and Halim M M 2023 *Optical Materials* **144** 114353
[45] Nayef U M, Hubeatir K A and Abdulkareem Z J 2016 *Optik* **127** 2806
[46] Nanda R K, Nath A, Singh L R and Sarkar M B 2023 *IEEE Transactions on Nanotechnology* **22** 769
[47] Ji T, Liu Q, Zou R, Sun Y, Xu K, Sang L, Liao M, Koide Y, Yu L and Hu J 2016 *Advanced Functional Materials* **26** 1400
[48] Ahmed A A, Hashim M R, Qahtan T F and Rashid M 2022 *Ceramics International* **48** 20078
[49] Sudha A, Ashok A, Patil S, Yadav S K and Swaminathan P 2023 *Solar Energy* **266** 112163